ACS NANO

www.acsnano.org

ARTICLE

Phase Engineering of Defective Copper Selenide toward Robust Lithium–Sulfur Batteries

Dawei Yang, Mengyao Li,* Xuejiao Zheng, Xu Han, Chaoqi Zhang, Jordi Jacas Biendicho, Jordi Llorca, Jiaao Wang,* Hongchang Hao, Junshan Li, Graeme Henkelman, Jordi Arbiol, Joan Ramon Morante, David Mitlin,* Shulei Chou,* and Andreu Cabot*

Cite This: *ACS Nano* 2022, 16, 11102–11114

Read Online

ACCESS | Metrics & More | Article Recommendations | Supporting Information

ABSTRACT: **The shuttling of soluble lithium polysulfides (LiPS) and the sluggish Li–S conversion kinetics are two main barriers toward the practical application of lithium–sulfur batteries (LSBs). Herein, we propose the addition of copper selenide nanoparticles at the cathode to trap LiPS and accelerate the Li–S reaction kinetics. Using both computational and experimental results, we demonstrate the crystal phase and concentration of copper vacancies to control the electronic structure of the copper selenide, its affinity toward LiPS chemisorption, and its electrical conductivity. The adjustment of the defect density also allows for tuning the electrochemically active sites for the catalytic conversion of polysulfide. The optimized S/$Cu_{1.8}Se$ cathode efficiently promotes and stabilizes the sulfur electrochemistry, thus improving significantly the LSB performance, including an outstanding cyclability over 1000 cycles at 3 C with a capacity fading rate of just 0.029% per cycle, a superb rate capability up to 5 C, and a high areal capacity of 6.07 mAh cm^{-2} under high sulfur loading. Overall, the present work proposes a crystal phase and defect engineering strategy toward fast and durable sulfur electrochemistry, demonstrating great potential in developing practical LSBs.**

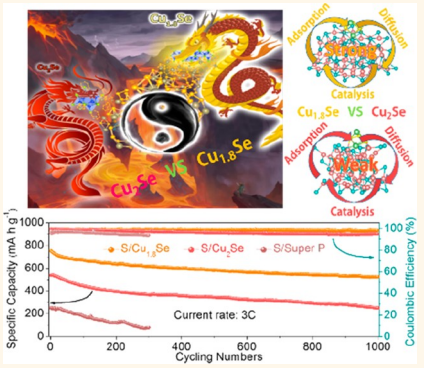

KEYWORDS: *copper selenide, phase engineering, copper vacancies, lithium–sulfur battery, lithium polysulfide*

Lithium–sulfur battery (LSB) has emerged as one of the most promising energy storage technologies owing to its large energy density (2600 Wh kg^{-1}) and high potential for low cost and environmental friendliness.[1−3] Despite these attractive advantages, the deployment of commercial LSBs is still hampered by several limitations, including the intrinsically low conductivity of sulfur and lithium sulfides, the dissolution and shuttling of lithium polysulfide (LiPS) intermediates, the large volume change of sulfur during the charge–discharge process, and the slow Li–S reaction kinetics, which result in insufficient cycling stabilities and rate capabilities.[4−6]

To address these issues, extensive efforts have been devoted to synthesizing porous/hollow carbon-based cathode hosts to physically confine sulfur and polysulfides.[7−10] However, the shuttle effect of soluble polysulfides cannot be effectively suppressed by means of carbon encapsulation due to the weak interaction of LiPS with nonpolar carbon materials.[11] Beyond encapsulation, a more effective strategy to suppress the shuttle effect is the use of sulfur host materials able to chemisorb and catalyze the LiPS reaction.[12,13] In this direction, several polar inorganic compounds including metal oxides,[14,15] nitrides,[16] phosphides,[17] and sulfides[18,19] have been incorporated into the host to chemically immobilize polysulfide species, accelerate their conversion, and thus reduce their dissolution and shuttling. Among the proposed compounds, transition metal chalcogenides (TMCs) have been demonstrated as particularly effective.[20−22]

Copper chalcogenides have recently drawn extensive attention as functional materials in several energy conversion and storage applications, including photovoltaics, thermoelectrics, and several electrochemical technologies.[23−25] The suitability of copper chalcogenides arises from the abundance

Received: April 18, 2022
Accepted: June 21, 2022
Published: June 27, 2022

https://doi.org/10.1021/acsnano.2c03788
ACS Nano 2022, 16, 11102–11114

Scheme 1. Schematic Illustration of the Synthetic Procedure Used to Produce Copper Selenide

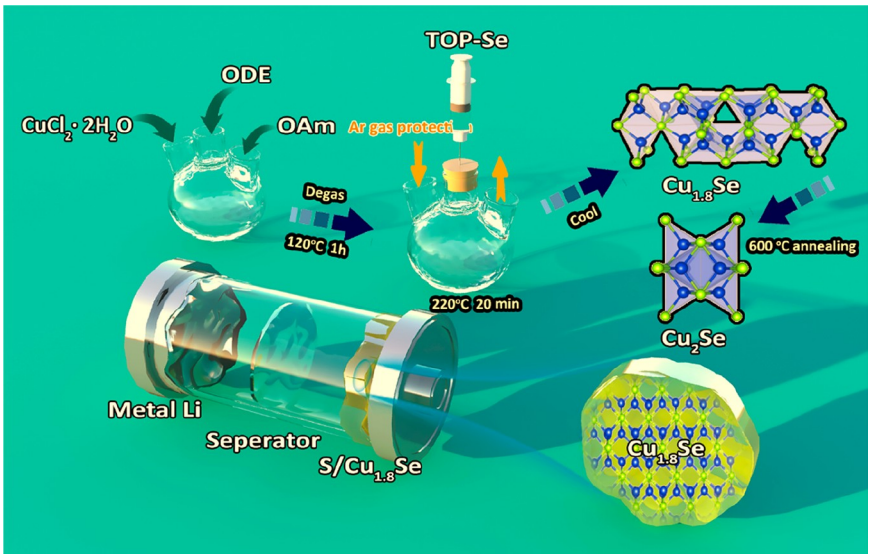

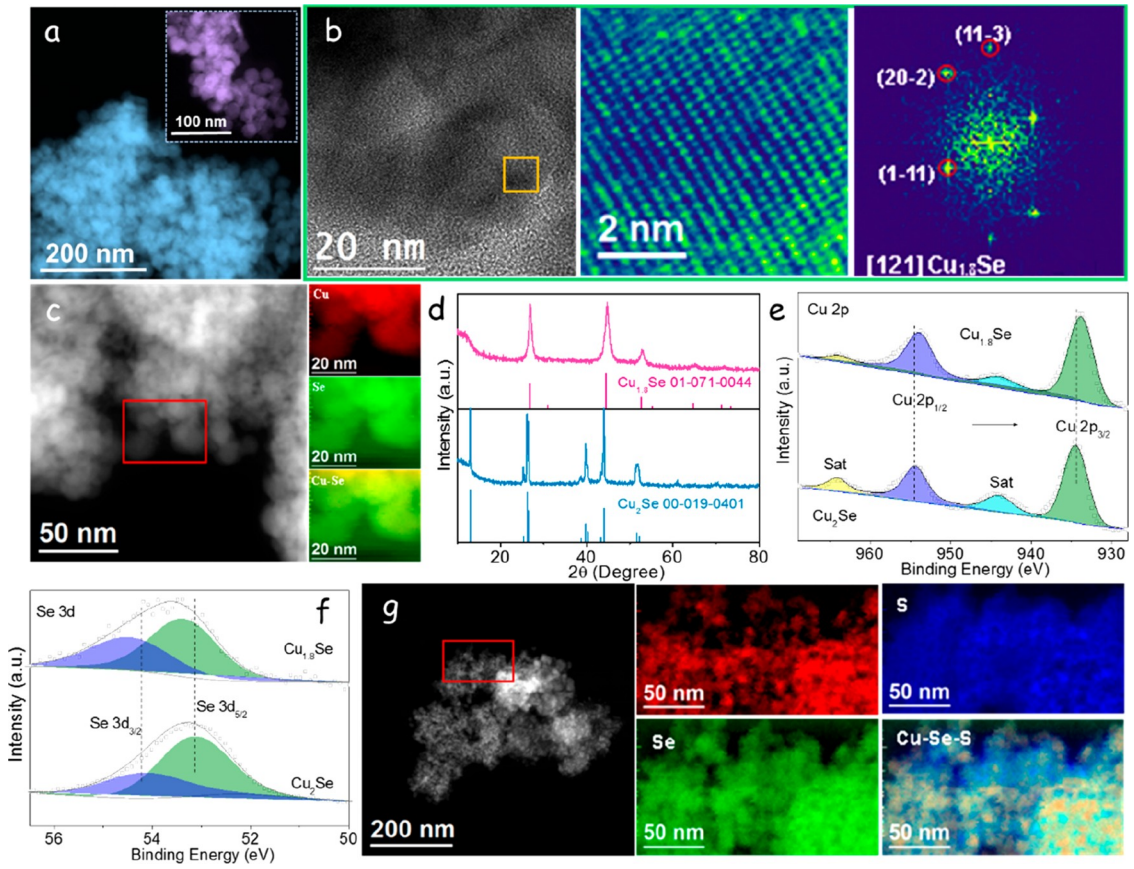

Figure 1. (a) TEM image of $Cu_{1.8}Se$. (b) HRTEM micrograph of $Cu_{1.8}Se$, detail of the orange squared region and its corresponding power spectrum. (c) EELS chemical composition maps obtained from the red squared area of the STEM micrograph of $Cu_{1.8}Se$. Individual Cu $L_{2,3}$-edges at 931 eV (red) and Se $M_{1,2}$-edges at 168 eV (green) and composites of Cu−Se. (d) XRD patterns of Cu_2Se and $Cu_{1.8}Se$. (e) Cu 2p and (f) Se 3d high-resolution X-ray photoelectron spectroscopy (XPS) spectra from Cu_2Se and $Cu_{1.8}Se$. (g) EELS chemical composition maps obtained from the STEM micrograph of a $S/Cu_{1.8}Se$ composite. Individual Cu $L_{2,3}$-edges at 931 eV (red) and Se $M_{1,2}$-edges at 168 eV (green), S $L_{2,3}$-edge 165 eV (blue) and composites of Cu−Se−S.

of their constituent elements, the strong influence of Cu 3d states on the electronic band structure near the Fermi level, the contribution of the redox reactions between Cu^0, Cu^{1+}, and Cu^{2+} to catalytically activating several processes, and the low defect formation energies that result in large densities of defects that control the optical, charge transport, and catalytic properties of the material.[26,27]

Among the different copper chalcogenides, sulfides offer advantages in terms of cost but are characterized by moderate electrical conductivities. At the other extreme, copper telluride

https://doi.org/10.1021/acsnano.2c03788
ACS Nano 2022, 16, 11102−11114

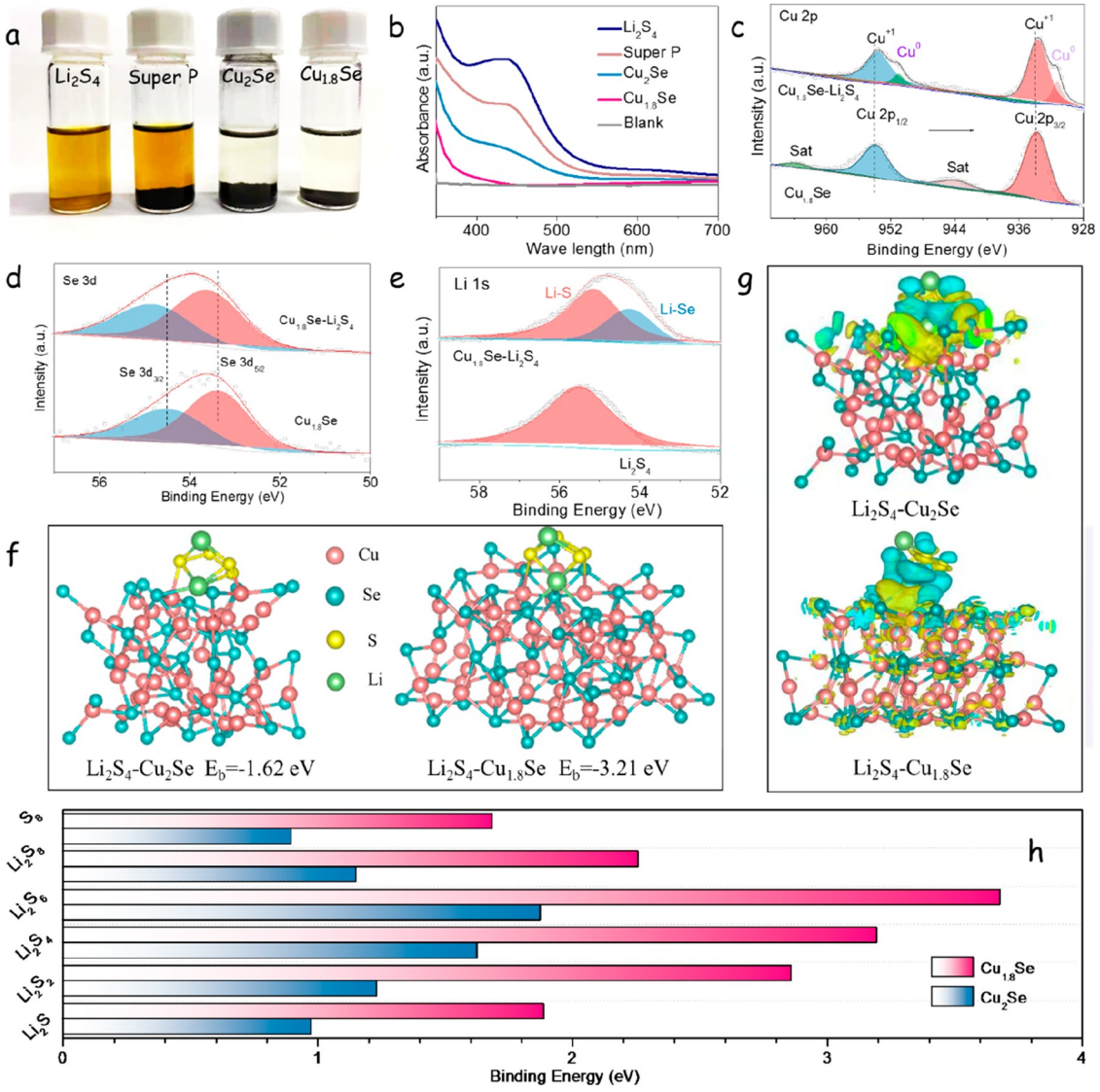

Figure 2. LiPS adsorption ability. (a) Optical image of $Cu_{1.8}Se$, Cu_2Se, and Super P materials soaked in Li_2S_4 solution after 12 h adsorption tests. (b) UV−vis spectrum of the absorbed Li_2S_4 solution containing the different adsorbents. (c−e) High-resolution XPS spectrum at (c) Cu 2p, (d) Se 3d, and (e) Li 1s core levels of the pristine $Cu_{1.8}Se$ and $Cu_{1.8}Se$−Li_2S_4, respectively. (f) Optimized adsorption configurations of LiPS species on the (220) facet of Cu_2Se and (111) facet of $Cu_{1.8}Se$, respectively. (g) Charge density difference of Li_2S_4 adsorbed on $Cu_{1.8}Se$ (111) and Cu_2Se (220). The yellow and cyan regions represent the accumulation and depletion of the electron, respectively. (h) Binding energies of LiPS species (Li_2S, Li_2S_2, Li_2S_4, Li_2S_6, Li_2S_8, and S_8) absorbed on $Cu_{1.8}Se$ and Cu_2Se surfaces, respectively, calculated with DFT.

shows a metallic character, but the low abundance of tellurium prevents its use in applications involving large volumes of material. Selenides thus represent the best compromise, as recognized in the fields of photovoltaics and thermoelectrics among others. Copper selenides have been also recently reported to show excellent electrocatalytic activity toward the oxygen reduction reaction among other electrocatalytic reactions.[28,29]

In the field of LSBs, copper sulfides have been explored as sulfur hosts able to expedite the polysulfides transformation, with notable success.[30−33] On the contrary, surprisingly, despite its high potential as LiPS adsorbent and Li−S electrocatalysts, no previous work on the use of copper selenides as a sulfur host in LSB cathodes has been reported.

Herein, we produced copper selenide electrocatalyst and optimized them toward the LiPS adsorption and catalytic conversion through adjusting their crystal phase and Cu vacancy concentration. Computational and experimental analyses are used to demonstrate that tailoring the crystal phase and defect concentration allows for modulating the electrical conductivity of the material, its chemical affinity toward LiPS adsorption, and its catalytic activity toward LiPS conversion reactions. The optimized materials are loaded with sulfur and tested as cathode material in LSBs, which capacity, stability, and rate capability are thoroughly investigated.

RESULTS AND DISCUSSION

A rapid synthetic protocol based on the injection of TOP-Se complex into a copper precursor solution at 220 °C was developed to produce the copper selenide NPs, as schematized in Scheme 1 (see details in the Experimental Section).

Figure 1a and Figure S1 display transmission electron microscopy (TEM) images of the 20 ± 10 nm quasi-spherical NPs obtained. Electron energy loss spectroscopy (EELS)

https://doi.org/10.1021/acsnano.2c03788
ACS Nano 2022, 16, 11102−11114

chemical composition maps displayed a uniform distribution of Cu and Se within each particle (Figure 1c). High-resolution TEM (HRTEM) characterization showed the crystal structure of the NPs to match the $Cu_{1.8}Se$ cubic phase (Figure 1b).[34] X-ray diffraction (XRD) patterns confirmed the cubic $Cu_{1.8}Se$ phase (JCPDS No. 01-071-0044, Figure 1d).[34]

$Cu_{1.8}Se$ NPs were annealed in a reducing atmosphere at 600 °C for 3 h. Parts a and b of Figure S2 display TEM and HRTEM images of the annealed material, which was characterized by larger crystal domains of a different phase identified as orthorhombic Cu_2Se.[35] XRD analysis confirmed the crystal structure of the annealed material to match that of orthorhombic Cu_2Se (JCPDS No. 00-019-0401, Figure 1d).[35] EELS chemical composition maps displayed a uniform distribution of Cu and Se within the Cu_2Se sample (Figure S2c).

Figure 1e displays the high-resolution Cu 2p XPS spectra of $Cu_{1.8}Se$ and Cu_2Se. A Cu 2p doublet was identified from both samples, and it was associated with Cu^+ within a copper selenide environment.[36] The Cu 2p doublet was located at 954.5 ($2p_{1/2}$) and 934.5 eV ($2p_{3/2}$) in Cu_2Se, and it was slightly shifted toward lower binding energies in $Cu_{1.8}Se$. The Se 3d XPS spectra of $Cu_{1.8}Se$ and Cu_2Se also displayed a single chemical state ascribed Se^{2-}, with a doublet located at 54.3 eV ($3d_{3/2}$) and 53.2 eV ($3d_{5/2}$) in the case of Cu_2Se and shifted to slightly higher energies in $Cu_{1.8}Se$ (Figure 1f).[37,38] The correlated red shift of the Cu 2p spectrum and blue shift of the Se 3d spectrum when decreasing the Cu/Se ratio from Cu_2Se to $Cu_{1.8}Se$ are associated with a transfer of charge from Se to Cu.

The electron paramagnetic resonance (EPR) spectra of Cu_2Se and $Cu_{1.8}Se$ were collected to characterize the oxygen vacancy concentration. As shown in Figure S3a, while the EPR spectrum of Cu_2Se showed no peak, the EPR spectrum of $Cu_{1.8}Se$ displayed an intense signal related to copper vacancies than. Besides, $Cu_{1.8}Se$ exhibited a relatively high electrical conductivity of 138.6 S cm^{-1}, well above that of Cu_2Se, 52.1 S cm^{-1}, as characterized by the four-point probe method (Figure S3b).

Sulfur was introduced within the host materials by a melt diffusion process (see the Experimental Section for details). XRD patterns (Figure S4) showed sulfur (JCPDS No. 01-85-0799) to be present in $S/Cu_{1.8}Se$.[39] EELS elemental maps displayed a homogeneous distribution of the three elements, Cu, Se, and S, within the composite (Figure 1g), with no independent sulfur particle. Nitrogen adsorption−desorption isotherms showed the Brunauer−Emmett−Teller (BET) specific surface area to be reduced from 64.3 m^2 g^{-1} for $Cu_{1.8}Se$ to 9.5 m^2 g^{-1} for $S/Cu_{1.8}Se$, which further demonstrated the successful loading of sulfur (Figure S5). Thermogravimetric analysis (TGA) allowed for quantifying the sulfur content in the $S/Cu_{1.8}Se$ composite at ca. 70.0 wt %, which matches well the nominal sulfur percentage incorporated (Figure S6).

LiPS adsorption affinity was evaluated by immersing the same amount of each of the hosts into a 0.01 M Li_2S_4 solution. After overnight incubation, the color of the solutions including the different adsorbers showed clear differences, as observed both by direct observation and using UV−vis spectroscopy, which denotes a different affinity to adsorb LiPS (Figure 2a,b). As observed from the optical images in Figure 2a, the 0.01 M Li_2S_4 solution had an intense orange color. In the presence of the carbon black Super P, the color of the solution remained unchanged after 12 h, as was expected from the low affinity of the nonpolar carbon surface to LiPS. On the contrary, the two solutions containing copper selenides displayed a much more pallid color, indicating that most of the Li_2S_4 in the solution had been captured by the adsorber. More precise conclusions can be obtained from the UV−vis spectra (Figure 2b). Li_2S_4 presents a strong absorption band in the range 400−500 nm.[40,41] The absorbance in this region strongly decreased in the presence of Cu_2Se, but especially with $Cu_{1.8}Se$, indicating a much stronger polysulfide adsorption ability of the latter.

The surface chemical states of $Cu_{1.8}Se$ after the Li_2S_4 adsorption test (labeled as $Cu_{1.8}Se-Li_2S_4$) were analyzed and compared with those of pristine $Cu_{1.8}Se$. Figure 2c displays the high-resolution Cu 2p XPS spectra of $Cu_{1.8}Se-Li_2S_4$. Compared with that of $Cu_{1.8}Se$, the Cu 2p spectrum of $Cu_{1.8}Se-Li_2S_4$ shifted toward lower binding energies, which is attributed to the less electronegative chemical environment created by the chemical adsorption of negatively charged polysulfide species on the $Cu_{1.8}Se$ surface.[42] Besides, a second Cu 2p doublet was identified in the Cu 2p spectra of $Cu_{1.8}Se-Li_2S_4$, at 951.2 and 931.3 eV, corresponding to the $2p_{1/2}$ and $2p_{3/2}$ levels of Cu^0. Thus, a partial reduction of the surface copper ions in $Cu_{1.8}Se$ took place during the LiPS chemisorption process.[36] Figure 2d shows the high-resolution Se 3d spectrum of $Cu_{1.8}Se$ before and after Li_2S_4 adsorption ($Cu_{1.8}Se-Li_2S_4$). Compared with pristine $Cu_{1.8}Se$, the Se 3d XPS spectrum of $Cu_{1.8}Se-Li_2S_4$ shifted to higher binding energies, which indicated an increase of the chemical environment electronegativity during the LiPS adsorption and simultaneous Cu partial reduction.[43,44] The Li 1s XPS spectra of $Cu_{1.8}Se-Li_2S_4$ is compared with that of Li_2S_4 in Figure 2e. While the Li 1s band at 55.2 eV is attributed to the Li−S bonding within Li_2S_4, the peak appearing in the Li 1s XPS spectra of $Cu_{1.8}Se-Li_2S_4$ is associated with the formation of Li−Se chemical bonds during the adsorption process.[45] Overall, the significant variations in the XPS spectra of $Cu_{1.8}Se$ before and after the Li_2S_4 adsorption test clearly demonstrate the chemical interaction and thus affinity between the $Cu_{1.8}Se$ surface and Li_2S_4.

DFT analyses were used to assess the LiPS binding energy on $Cu_{1.8}Se$ and Cu_2Se surfaces. The calculated geometrically stable configurations of $Cu_2Se-Li_2S_4$ and $Cu_{1.8}Se-Li_2S_4$ are illustrated in Figure 2f. The results revealed that the S and Li atoms in Li_2S_4 preferentially bind with the Cu and Se atoms on the (002) surface of Cu_2Se and (111) surface of $Cu_{1.8}Se$, respectively. While in both cases negative binding energies were obtained, a significantly higher absolute value of the binding energy (−3.21 eV) is achieved for $Cu_{1.8}Se-Li_2S_4$ than for $Cu_2Se-Li_2S_4$ (−1.62 eV), which is consistent with the Li_2S_4 test results.

To gain additional insight into the interactions between LiPS species and copper selenide surfaces, the charge density difference of Li_2S_4 species adsorbed on Cu_2Se (220) and $Cu_{1.8}Se$ (111) were calculated and are displayed in Figure 2g. The cyan isosurfaces around the Li−S bonds in Li_2S_4 indicated a decreased charge density and weakened bonds between Li and S atoms, which benefits its further conversion toward lower-order LiPS. In addition, the yellow isosurface suggests that the charge density between $Cu_{1.8}Se$ and the Li atom of Li_2S_4 was significantly increased, indicating a strong interaction between $Cu_{1.8}Se$ and Li_2S_4, which is consistent with the stronger affinity of the $Cu_{1.8}Se$ surfaces to LiPS.[46]

https://doi.org/10.1021/acsnano.2c03788
ACS Nano 2022, 16, 11102−11114

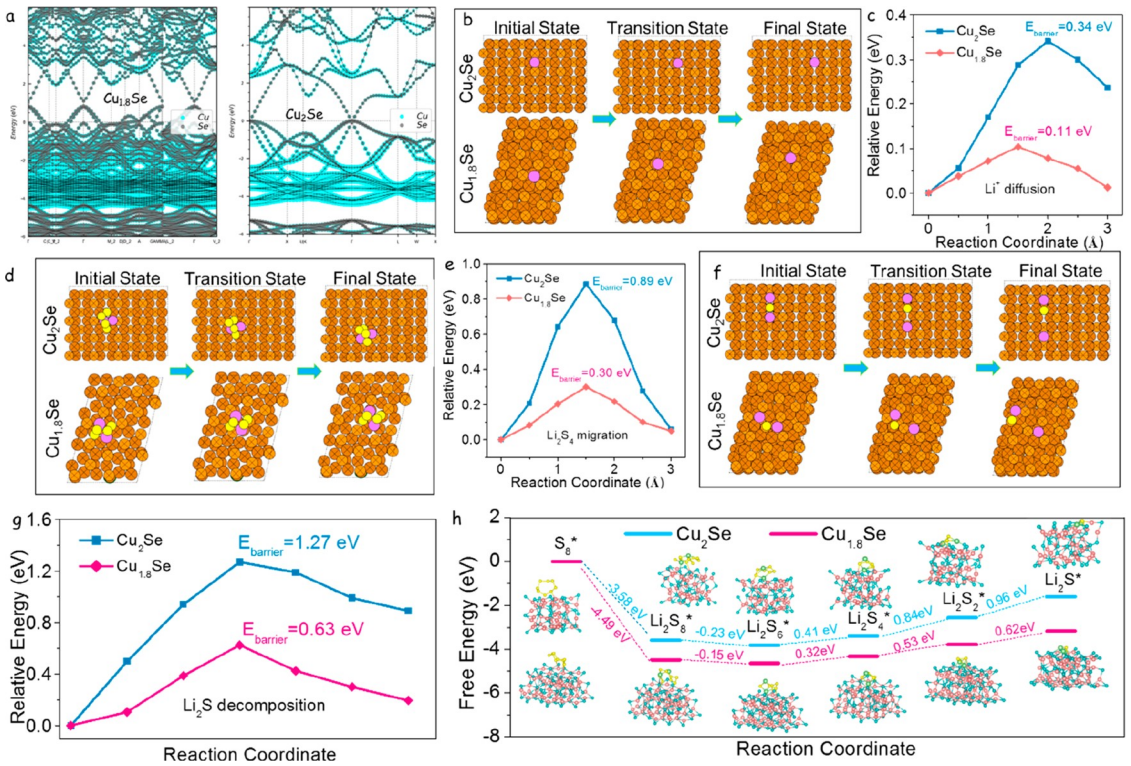

Figure 3. Lithium-ion diffusion and catalytic conversion kinetics studies of polysulfides in Li−S cells. (a) HSE06 band structures of Cu_2Se and $Cu_{1.8}Se$, respectively. (b) Total Li-ion diffusion paths on the optimized (220) facet of Cu_2Se and (111) facet of $Cu_{1.8}Se$, respectively. (c) Energy barrier of Li-ion diffusion on (220) facet of Cu_2Se and (111) facet of $Cu_{1.8}Se$, respectively. (d) Illustration of stages of Li_2S_4 diffusing on (002) facet of Cu_2Se and (111) facet of $Cu_{1.8}Se$, respectively. (e) Energy profiles of Li_2S_4 migration on (002) facet of Cu_2Se and (111) facet of $Cu_{1.8}Se$ along different adsorption sites. (f) Initial state, transition state, and final state of Li_2S decomposition on (220) facet of Cu_2Se and (111) facet of $Cu_{1.8}Se$, respectively. (g) Energy barrier profiles of Li_2S cluster decomposition on Cu_2Se and $Cu_{1.8}Se$ along with different reaction coordinates. (h) Gibbs free energy profiles of LiPS species on Cu_2Se and $Cu_{1.8}Se$, showing a lower reaction free energy from Li_2S_2 to Li_2S on $Cu_{1.8}Se$ than that on Cu_2Se.

The results of computational simulations of the interactions between Cu_xSe and different LiPS covering the full range of sulfur chemical states upon battery operation (Li_2S, Li_2S_2, Li_2S_4, Li_2S_6, Li_2S_8, and S_8) are displayed in Figures S7 and S8. The S−Cu and Li−Se attractions can be confirmed and are maintained in all the LiPS-adsorbent couples, while $Cu_{1.8}Se$ exhibits stronger adsorbability for the LiPS by showing systematically higher binding energies (Figure 2h) and shorter bond lengths for both the S−Cu and Li−Se bonds than Cu_2Se (Figure S9).

DFT results showed the $Cu_{1.8}Se$ Fermi level to lay within a band of states, which was consistent with its degenerated/metallic character and is related to the high density of Cu vacancies that provide high hole densities.[38,47] In contrast, the Fermi level of Cu_2Se lies within its bandgap showing a p-type semiconductor behavior (Figure 3a).

DFT calculations were also used to evaluate the lithium-ion and Li_2S_4 diffusion on the (002) facet of Cu_2Se and the (111) facet of $Cu_{1.8}Se$. The geometrical configurations of the Li-ion diffusion paths are shown in Figure 3b, and the corresponding energy profiles are displayed in Figure 3c. The calculated Li-ion diffusion energy barriers ($E_{barrier}$) were relatively low, just 0.34 eV for Cu_2Se and even a 3-fold smaller, 0.11 eV, for $Cu_{1.8}Se$. Parts d and e of Figure 3 displays the geometrical configurations of the path for Li_2S_4 migration on the (002) facet of Cu_2Se and the (111) facet of $Cu_{1.8}Se$ and the $E_{barrier}$ for Li_2S_4 migration along different adsorption sites. Calculations showed the $E_{barrier}$ for Li_2S_4 migration on Cu_2Se to be 0.89 eV and just 0.30 eV on $Cu_{1.8}Se$. These low diffusion barriers allow fast Li-ion and LiPS diffusion rates on the copper selenide surfaces, which promotes the Li−S redox reactions.

Figure 3f exhibits the initial state, transition state, and final state of Li_2S decomposition on the basis of different sulfur hosts. The calculated energy barriers for Li_2S decomposition on Cu_2Se and $Cu_{1.8}Se$ surface S were 1.27 and 0.63 eV, respectively (Figure 3g). Thus, the defective cubic $Cu_{1.8}Se$ can greatly reduce the Li_2S decomposition energy barrier and enhance the redox reversibility between Li_2S and LiPS.

The calculated Gibbs free energy changes during the S reduction on Cu_2Se and $Cu_{1.8}Se$ are displayed in Figure 3h. The overall reversible reaction from S_8 and Li to Li_2S was considered. During the discharge process, the first step involves the double reduction of S_8 with two Li^+ to form Li_2S_8. Then, Li_2S_8 undergoes further reduction to three intermediate LiPS, Li_2S_6, Li_2S_4, and Li_2S_2. Finally, Li_2S is obtained as the end product. The largest increase of Gibbs free energy was obtained for the conversion from Li_2S_2 to Li_2S, suggesting this step as the rate-limiting one during the discharge process.[48,49] Both copper selenides exhibited low Gibbs free energy changes, demonstrating their potential as Li−S catalysts. Among them, $Cu_{1.8}Se$ was characterized with the lowest Gibbs free energy change, 0.62 eV, well below that of Cu_2Se, 0.96 eV, which suggests that the reduction of S is more thermodynamically favorable on $Cu_{1.8}Se$ than on Cu_2Se. Overall, DFT calculations pointed at the defective cubic

https://doi.org/10.1021/acsnano.2c03788
ACS Nano 2022, 16, 11102−11114

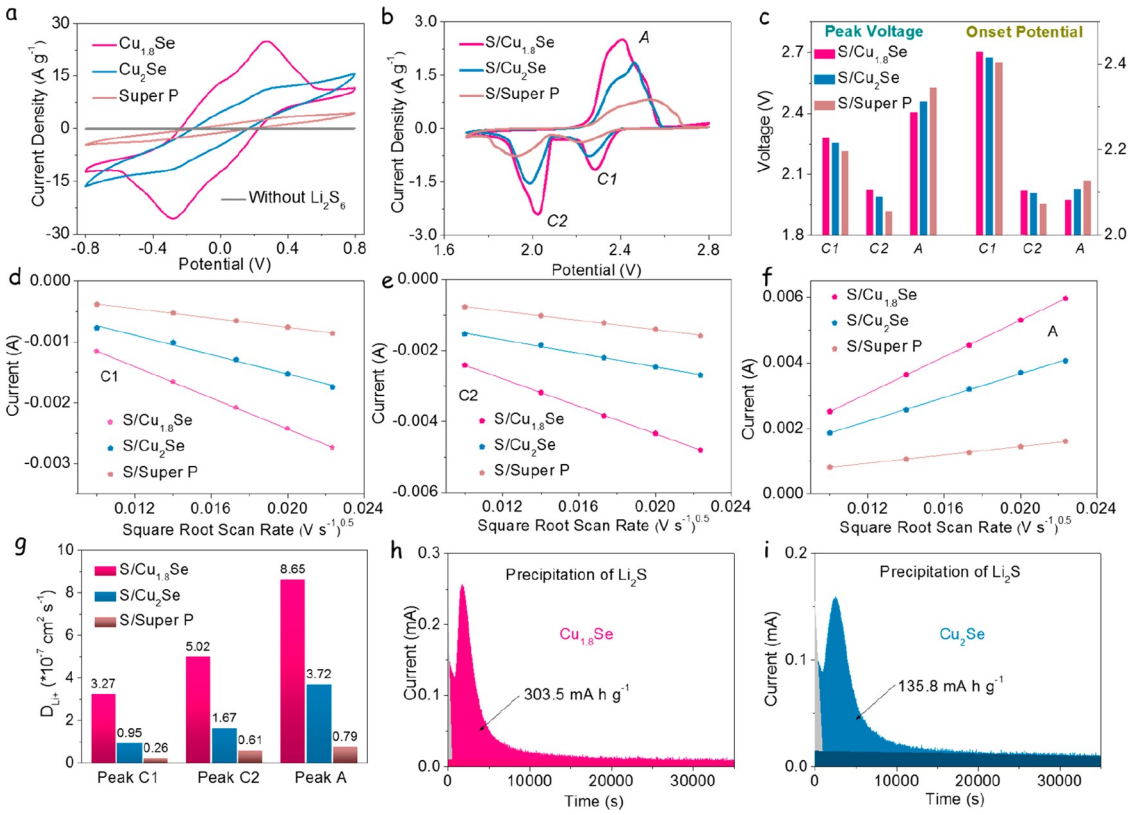

Figure 4. (a) CV profiles of symmetrical cells at a scan rate of 20 mV s^{-1} with $Cu_{1.8}Se$, Cu_2Se, and Super P host materials. (b) CV curves of Li−S cells with different electrodes. (c) Peak voltages and onset potentials based on the CV curves of Li−S coin cells. (d−f) CV peak current values of peaks C1, C2, and A for S/$Cu_{1.8}Se$, S/Cu_2Se, and S/Super P electrodes versus the square root of scan rates. (g) Li^+ diffusion coefficient value at peaks C1, C2, and A. (h and i) Potentiostatic discharge profile at 2.05 V with Li_2S_8 catholyte for evaluating the nucleation kinetics of Li_2S on $Cu_{1.8}Se$ and Cu_2Se electrodes.

$Cu_{1.8}Se$ structure as the most effective to trap LiPS and catalytically accelerate the Li−S reversible reaction.

Cyclic voltammetry (CV) on symmetrical cells was used to experimentally determine the catalytic activity of the different host materials. For these analyses, we used Li_2S_6 as LIPS and a voltage window −0.8 to +0.8 V. Electrodes based on $Cu_{1.8}Se$, Cu_2Se, and Super P displayed notable differences (Figure 4a). $Cu_{1.8}Se$ electrodes resulted in larger peak current densities than Cu_2Se and Super P electrodes, which illustrated the faster reaction kinetics of $Cu_{1.8}Se$ during liquid-to-solid ($Li_2S \leftrightarrow S_6^{2-} \leftrightarrow S_8$) conversion.[20,50] When similar experiments were carried out on $Cu_{1.8}Se$ electrodes without Li_2S_6 addition in the electrolyte, approximately linear CV curves were measured, pointing at a pure capacitive behavior, implying Li_2S_6 to be the sole electrochemically active specy. The well-maintained CV profile of symmetric cells based on $Cu_{1.8}Se$ after 10 cycles points at proper reaction stability (Figure S10).

Coin-type cells were used to further evaluate the electrochemical performance of the electrodes. Figure 4b displays the CV profiles of Li−S cells based on S/$Cu_{1.8}Se$, S/Cu_2Se and S/Super P cathodes at a scan rate of 0.1 mV s^{-1}. All curves displayed two reduction peaks (peak C1 and C2) that were attributed to a S reduction in two steps: peak C1 was associated with the reaction of sulfur to long-chain LiPS (Li_2S_x, $4 \leq x \leq 8$) and peak C2 to a further reduction of sulfur to insoluble Li_2S_2/Li_2S.[19,51] The anodic peak (peak A) corresponded to the multiple-step oxidation of short-chain sulfides to sulfur.[52] S/$Cu_{1.8}Se$ electrodes were characterized by the largest peak currents and the most positive/negative potentials of the cathodic/anodic peaks (Figure 4c). Therefore, among the tested materials, $Cu_{1.8}Se$ stood out as the most active catalyst for the polysulfides redox reaction.

The excellent catalytic activity of $Cu_{1.8}Se$ was further confirmed by measuring the onset potentials at a current density of 10 μA cm^{-2} beyond the baseline current (Figure S11).[52,53] As illustrated in Figure 4c, among the three electrodes tested, S/$Cu_{1.8}Se$ exhibited the highest onset potentials of reduction peaks and the lowest onset potentials of oxidation peaks, evidencing the ability of $Cu_{1.8}Se$ to reduce the overpotentials of the Li−S reversible reaction. Besides, the CV curves of S/$Cu_{1.8}Se$ almost overlapped, showing no obvious peak shift or current changes, which points to excellent stability and reversibility (Figure S12).

The lithium-ion (Li^+) diffusion rate, which is another important factor affecting the conversion kinetics of LiPSs, was investigated using CV curves at variable rates, from 0.1 to 0.5 mV s^{-1}. Figure S13 displays the results obtained from S/$Cu_{1.8}Se$, S/Cu_2Se, and S/Super P electrodes containing similar amounts of sulfur. All reduction and oxidation peaks current were observed to linearly change with the square root of the scan rates, demonstrating the reaction to be diffusion-limited. Thus, the Li^+ diffusivity can be estimated according to the classical Randles−Sevcik equation:[40,54]

$$I_p = (2.69 \times 10^5) n^{1.5} A D_{Li^+}{}^{0.5} C_{Li^+} \nu^{0.5}$$

where I_p is the peak current density, n is the number of reaction electrons, A is the geometric area of the electrode,

https://doi.org/10.1021/acsnano.2c03788
ACS Nano 2022, 16, 11102−11114

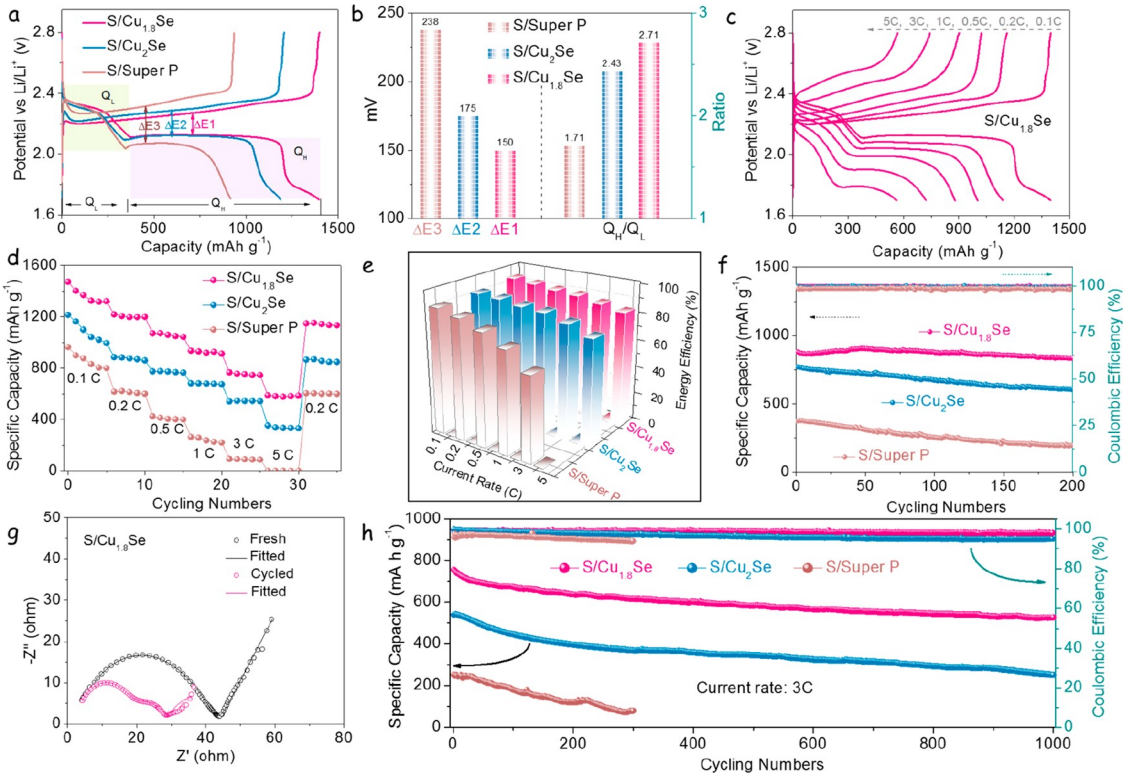

Figure 5. (a) Galvanostatic charge/discharge profiles of $S/Cu_{1.8}Se$, S/Cu_2Se, and S/Super P electrodes at a current rate of 0.1 C. (b) ΔE and Q_H/Q_L values obtained from charge/discharge curves. (c) Charge/discharge curves of the $S/Cu_{1.8}Se$ electrodes at various C rates from 0.1 to 5 C. (d) Rate capabilities of $S/Cu_{1.8}Se$, S/Cu_2Se, and S/Super P electrodes at various C rates from 0.1 to 5 C. (e) Energy efficiencies of three different electrodes at different current densities. (f) Cycling performances of different electrodes at 1 C over 200 cycles. (g) EIS spectrum of $S/Cu_{1.8}Se$ electrode after and before 200 cycles at 1 C. (h) Long-term cycling behavior of Li−S cells based on $S/Cu_{1.8}Se$, S/Cu_2Se, and S/Super P electrodes at 3 C.

D_{Li+} is the Li^+ diffusion coefficient, C_{Li+} is the concentration of Li^+ in the electrolyte, and ν is the scan rate.

As shown in Figure 4d−f, $S/Cu_{1.8}Se$ electrodes exhibited the sharpest slopes for the three peaks (peak C1, peak C2, and peak A) and, thus, the highest Li^+ diffusivity during the redox reactions. On the basis of the Randles−Sevcik equation, $S/Cu_{1.8}Se$ electrodes were characterized by D_{Li+} at peaks C1, C2, and A of 3.3×10^{-7}, 5.0×10^{-7}, and 8.6×10^{-7} cm^2 s^{-1}, respectively, well above the values obtained for S/Cu_2Se and S/Super P (Figure 4g). The Li^+ diffusivity strongly depends on the accumulation of insulating Li_2S/Li_2S_2 on the electrode and the viscosity of the electrolyte that varies with the concentration of soluble LiPS.[52] The highest Li^+ diffusivities obtained for the $Cu_{1.8}Se$ host reflect a more effective catalytic activity toward Li−S reaction and a more effective trapping of soluble LiPS that prevented them from dissolving into the electrolyte.

A very significant part of the discharge capacity, up to 75%, stems from the transformation of the Li_2S_4 intermediate into Li_2S. Thus, the rate of Li_2S precipitation on the electrode matrix is a very significant conversion kinetic indicator for LSBs. From the potentiostatic discharge profiles in Figure 4h,i, both copper selenide electrodes displayed very sharp nucleation peaks and fast responsivity toward Li_2S nucleation, being the $Cu_{1.8}Se$ performance significantly better than that of the Cu_2Se electrodes. According to Faraday's law, the Li_2S deposition capacity of $Cu_{1.8}Se$ (304 mAh g^{-1}) was larger than that of Cu_2Se (136 mAh g^{-1}).

Galvanostatic charge/discharge curves of $S/Cu_{1.8}Se$, S/Cu_2Se, and S/Super P at 0.1 C (1 C = 1672 mA g^{-1}) exhibited one charge plateau and two discharge plateaus (Figure 5a), consistently with CV. The voltage gap between the charge plateaus and the second discharge is generally referred to as the polarization potential (ΔE).[55] As displayed in Figure 5b, $S/Cu_{1.8}Se$ electrodes showed a lower polarization potential (ΔE = 150 mV) than S/Cu_2Se (ΔE = 175 mV) and S/Super P electrodes (ΔE = 238 mV).

The host material catalytic activity was further quantified by the Q_H/Q_L ratio, where Q_L and Q_H are the capacities of each of the discharge plateaus (Figure 5a). Q_L is related to the reduction of sulfur to soluble LiPS ($S_8 + 4Li^+ + 4e^- \rightarrow 2Li_2S_4$) and Q_H corresponds to the subsequent transformation to insoluble sulfide ($2Li_2S_4 + 12Li^+ + 12e^- \rightarrow 8Li_2S$).[48] Thus, the ratio Q_H/Q_L can be interpreted in terms of the catalytic ability for LiPS conversion reaction: sluggish kinetics during the solid → liquid → solid process and shuttle effect caused by the diffusion of soluble LiPS give rise to capacity fading during the Q_H stage. Thus, the higher Q_H/Q_L, the better the catalytic ability. As shown in Figure 5b, Q_H/Q_L ratios obtained for copper selenides were much larger than those of the carbon black (Q_H/Q_L = 1.71), being that the Q_H/Q_L ratio of the $S/Cu_{1.8}Se$ electrode (Q_H/Q_L = 2.71) is significantly larger than that of S/Cu_2Se (Q_H/Q_L = 2.43).

The electrochemical kinetics were further analyzed during the phase transformation between soluble LiPS and insoluble Li_2S_2/Li_2S in the charge/discharge processes. Figure S14a shows the voltage jump at the initial charging period, reflecting

https://doi.org/10.1021/acsnano.2c03788
ACS Nano 2022, 16, 11102−11114

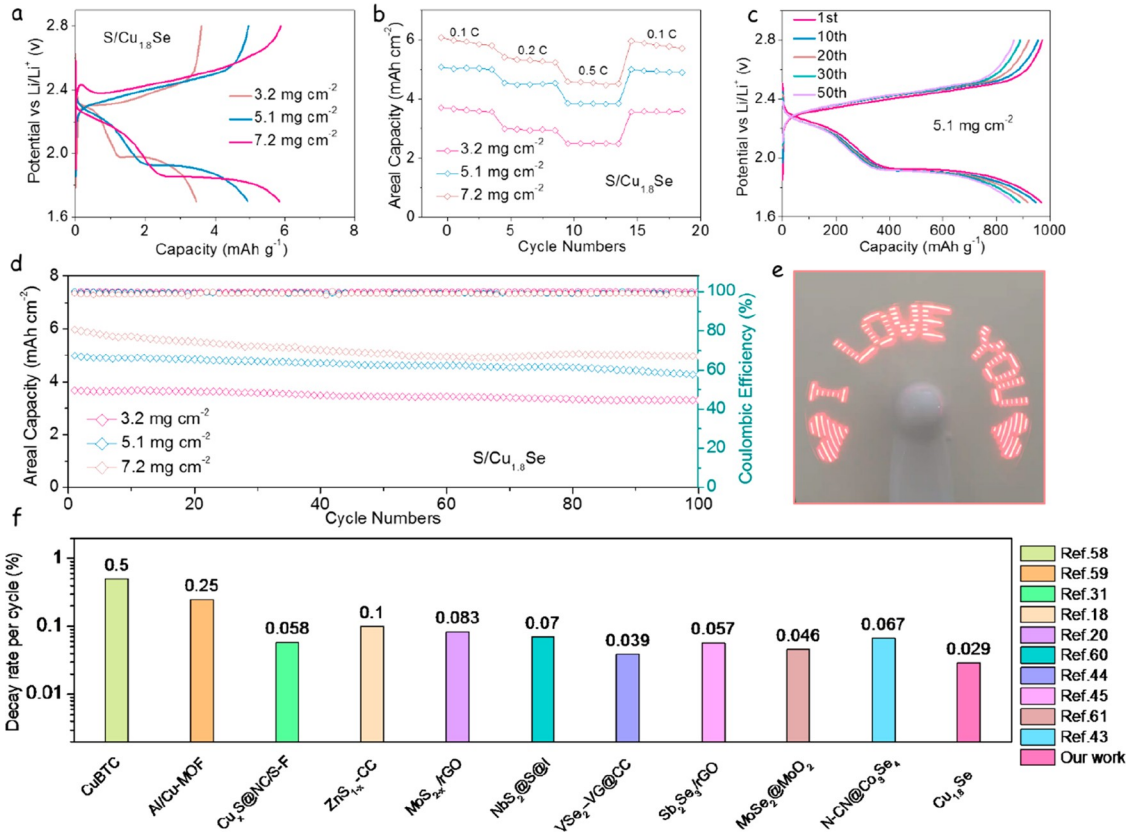

Figure 6. (a) Charge/discharge profiles at 0.1 C of $S/Cu_{1.8}Se$ electrodes under raised sulfur loadings of 3.2, 5.1, and 7.2 mg cm^{-2}. (b) Rate capabilities with different sulfur loadings at various current densities. (c) Galvanostatic charge/discharge profiles at 0.1 C with a sulfur loading of 5.1 mg cm^{-2}. (d) High-loading cycling performances with sulfur loadings of 3.2, 5.1, and 7.2 mg cm^{-2} at 0.1 C of $S/Cu_{1.8}Se$ electrodes. (e) Photograph of an electric fan with an "I LOVE YOU" pattern being charged by Li−S cells based on $S/Cu_{1.8}Se$ electrodes. (f) Decay rate per cycle compared with other reported works.

the overpotentials of Li_2S activation.[9] Besides, the galvanostatic discharge curves displayed a voltage dip at the beginning of the Li_2S precipitation voltage plateaus, which is associated with the overpotential of Li_2S nucleation (Figure S14b).[38] In both charge and discharge processes, the $S/Cu_{1.8}Se$ electrode exhibited lower overpotentials than S/Cu_2Se and S/Super P electrodes, indicating a promoted Li−S reaction.

The galvanostatic charge/discharge profiles of $S/Cu_{1.8}Se$, S/Cu_2Se, and S/Super P electrodes at various current densities, from 0.1 to 5 C, are displayed in Figure 5c and Figure S15. Figure 5d compares the rate performances of the different electrodes. Copper selenide electrodes displayed significantly higher capacities than carbon black. The $S/Cu_{1.8}Se$ electrode showed the largest capacity among the different electrodes tested, with two clear discharge plateaus at all current rates. The $S/Cu_{1.8}Se$ electrode displayed the best rate capability with a high capacity of 1218 mAh g^{-1} at 0.2 C and 588 mAh g^{-1} at 5 C. When switched back to 0.2 C, the capacity recovered to 1148 mAh g^{-1}, corresponding to 94.3% of its initial value, indicating good electrochemical reversibility. In comparison, the cells based on S/Super P undergo rapid capacity fading when increasing the current rate to 5 C. The excellent rate capability of the copper selenides, especially the $S/Cu_{1.8}Se$ electrode, is consistent with their high ability to accelerate the charge transfer and promote the conversion of polysulfides.

The energy conversion efficiency of the cells in the charge/discharge process was determined by the energy output/input ratio ($E = \int UIdt$).[40,56] At a rate of 0.1 C, the different electrodes displayed notable energy efficiencies ca. 90% (Figure 5e). At higher current rates, $S/Cu_{1.8}Se$ was characterized by the most stable and the largest energy efficiency, with 88.5% efficiency at 1 C and 82.8% at 5 C. In contrast, the S/Super P electrode was characterized with just a 71.3% efficiency at 1 C. The high energy efficiency of the cathodes based on copper selenides, and particularly the $S/Cu_{1.8}Se$ electrode, is associated with their low polarization potential and excellent catalytic activity.

Figure 5f displays the galvanostatic cycling performances of coin cells with different cathodes. Consistent with previous results, the $S/Cu_{1.8}Se$ electrode enabled a high initial capacity of 882 mAh g^{-1} at 1 C and 837 mAh g^{-1} after 200 cycles, which corresponds to an outstanding capacity retention of 94.9%. The S/Cu_2Se electrode also showed a notable initial capacity (770 mAh g^{-1}) and decent capacity retention of ca. 80% after 200 cycles. In contrast, the S/Super P electrode showed a moderate initial capacity (375 mAh g^{-1}) and low capacity retention (52.8%) after 200 cycles.

Figure 5g and Figure S16 display the Nyquist plot of the electrochemical impedance spectroscopy (EIS) data obtained from $S/Cu_{1.8}Se$, S/Cu_2Se, and S/Super P coin cells before and after cycling at 1 C. For the fresh electrodes, the semicircle in the high-frequency region is related to the charge-transfer resistance (R_{ct}), and the linear feature in the low-frequency region is associated with the diffusion of lithium ions.[52,57] On the basis of the equivalent circuit shown in Figure S16c, a relatively low R_{ct} was obtained for the $S/Cu_{1.8}Se$ electrodes

https://doi.org/10.1021/acsnano.2c03788
ACS Nano 2022, 16, 11102−11114

(39.5 Ω), well below that of S/Cu_2Se (71.3 Ω) and S/Super P (87.8 Ω). After 200 charge/discharge cycles at 1 C, an additional semicircle in the high-frequency range was evidenced. This feature is associated with the resistance of an insoluble Li_2S_2/Li_2S passivation layer (R_p in the equivalent circuit shown in Figure S16d) grown during cycling. After cycling, the S/$Cu_{1.8}Se$ electrodes were characterized by smaller R_{ct} (9.8 Ω) and R_p (16.1 Ω), than S/Cu_2Se (R_{ct} = 32.5 Ω, R_p = 22.9 Ω) and S/Super P (R_{ct} = 53.5 Ω, R_p = 109 Ω) (Figure S17). This result confirms the important role played by copper selenides and particularly $Cu_{1.8}Se$ in accelerating the LiPS conversion reaction and facilitating the charge transfer kinetics during lithiation/delithiation reactions.

Figure 5h displays the long-term cycling performance of the electrodes at 3 C. Copper selenide electrodes displayed an excellent cycling performance at this relatively high current rate, well above that of the cell based on a carbon cathode. Among the two copper selenides tested, the highly defective cubic $Cu_{1.8}Se$ showed the best cyclability, retaining a high reversible capacity of 527 mAh g^{-1} after 1000 cycles at 3 C, which corresponds to a tiny capacity fading rate of 0.029% per cycle. It is worth mentioning that a negligible capacity was obtained from pure u-NCSe under the same measuring conditions, as shown in Figure S18. The outstanding capacity, rate capability, and cyclability of the $Cu_{1.8}Se$ cathodes are attributed to the highly conductive nature, rapid ion transfer, excellent catalytic activity, and good LiPS affinity of this material, which immobilizes LiPS species and effectively accelerate their electrochemical conversion.

A key step toward the real-world application of LSBs is increasing the sulfur loading to rise the energy density of the overall device. Thus, the performance of S/$Cu_{1.8}Se$ cathodes with higher sulfur loadings of 3.2, 5.1, and 7.2 mg cm^{-2} was also evaluated. As shown in Figure 6a, at a 0.1 C current rate, a two-plateau voltage profile is discerned under high of the highest sulfur loadings tested, up to 7.2 mg cm^{-2}, with a high areal capacity of 6.07 mAh cm^{-2}, which largely exceeds the industrially requested areal capacity of LIBs (~4 mAh cm^{-2}). S/$Cu_{1.8}Se$-based cells containing high sulfur loads also demonstrated a notable rate performance (Figure 6b), achieving areal capacities of 3.01, 4.54, and 5.40 mAh cm^{-2} at 0.2 C when containing 3.2, 5.1, and 7.2 mg cm^{-2} of sulfur, respectively. As shown in Figure 6c, the high sulfur loaded Li–S cells based on S/$Cu_{1.8}Se$ cathodes also showed a notably stable Li–S electrochemistry, with just a slight potential hysteresis after 50 cycles that indicates a minor LiPS shuttling. Figure 6d displays the cycling performances of the high sulfur loaded cells. S/$Cu_{1.8}Se$ cathodes showed high capacity retention after 100 cycles, with areal capacities of 3.32, 4.27, and 5.00 mAh cm^{-2} at sulfur loadings of 3.2, 5.1, and 7.2 mg cm^{-2}, respectively.

As a practical demonstration of the potential of LSB cells based on $Cu_{1.8}Se$ cathodes, an electric fan with a light pattern was powered with a single coin cell (Figure 6e). Besides, the excellent performance of $Cu_{1.8}Se$-based cathodes is placed in context in Figure 6f and Table S1, where results obtained in the present work are compared with those reported in previous publications.

CONCLUSIONS

In summary, we demonstrated copper selenides produced by a facile solution-based method to be an efficient multifunctional sulfur host material in LSB cathodes. Both experimental results and computational data demonstrated the excellent electrochemical performance of copper selenides, and particularly $Cu_{1.8}Se$, to be attributed to (i) the presence of a combination of lithiophilic/sulfiphilic sites, which contributes to an effective trapping of LiPS and the related promotion of the Li^+ diffusion; (ii) high electrical conductivity of $Cu_{1.8}Se$ associated with its high density of copper vacancies; and (iii) a large improvement of the Li–S reaction kinetics during the battery charge/discharge processes, including LiPS phase change and Li_2S deposition/dissolution. Among the copper selenides tested, experimental data and DFT calculations pointed at the defective cubic $Cu_{1.8}Se$ structure as the most effective to trap LiPS and to catalytically accelerate the Li–S reversible reaction. Attributed to these beneficial features, S/$Cu_{1.8}Se$ cathodes delivered excellent long-term cycling stability with a low capacity fading of 0.029% per cycle over 1000 cycles, an excellent rate capability up to 5 C, and a high areal capacity of 6.07 mAh cm^{-2} under a high sulfur load (7.2 mg cm^{-2}). This work demonstrates that multifunctional sulfur hosts, with high adsorption and catalytic capabilities for rapid LPS adsorption-conversion process, hold a great promise in promoting the practical application of LSBs.

EXPERIMENTAL SECTION

Chemicals. Copper(II) chloride dihydrate ($CuCl_2·2H_2O$, 99+%), selenium pieces (99.999%), and 1-octadecene (ODE, technical grade 90%) were purchased from Aldrich. Trioctylphosphine (TOP, 97%) was purchased from Strem Chemicals. Oleylamine (OAm, C18 content approximately 80–90%) was purchased from Fisher. Analytical grade ethanol and hexane were obtained from various sources. All chemicals were used as received, without further purification. A stock solution of TOP-Se (1 M) was prepared by dissolving 0.789 g of selenium pieces in 10 mL of TOP. All syntheses were carried out using standard vacuum/argon Schlenk lines.

Synthesis of $Cu_{1.8}Se$ and Cu_2Se. In a typical synthesis, 9 mmol of $CuCl_2·2H_2O$ was mixed with 30 mL of ODE and 70 mL of OAm in a 250 mL three-neck flask. The mixture was degassed under a vacuum for 20 min at room temperature and then heated to 120 °C for 1 h under a vacuum. Afterward, the solution was flushed with Ar and heated to 220 °C. At this temperature, 5 mL of the TOP-Se stock solution was quickly injected. After injection, the reaction temperature was maintained at 220 °C for 20 min. Then, the solution was cooled using a water bath. $Cu_{1.8}Se$ nanoparticles (NPs) were precipitated and redispersed several times using ethanol and hexane. Then, $Cu_{1.8}Se$ NPs were dried under a vacuum and kept in an Ar-filled glovebox until their posterior use. Cu_2Se was obtained by annealing the $Cu_{1.8}Se$ NPs under a reducing atmosphere (5% H_2 in Ar) at 600 °C for 3 h.

Synthesis of S/$Cu_{1.8}Se$, S/Cu_2Se, and S/Super P. Typically, $Cu_{1.8}Se$ and sulfur powder were mixed with a weight ratio of 1:3, and then, the mixture was heated at 155 °C for 8 h in a sealed glass bottle under Ar protection. Then, the powder was immersed in a 10 mL CS_2 and ethanol solution (1:4, volume ratio) several times to remove the redundant sulfur not incorporated into $Cu_{1.8}Se$. S/Cu_2Se and S/Super P were prepared by the same method.

Materials Characterization. X-ray diffraction (XRD) patterns were obtained using a Bruker AXS D8 Advance X-ray diffractometer with Cu K radiation (λ = 1.5106 Å) operating at 40 kV and 40 mA. The morphology and microstructure of samples were characterized in ZEISS Auriga Field emission scanning electron microscopy (FESEM) equipped with an energy-dispersive X-ray spectroscopy (EDS) detector operated at 20 kV. Transmission electron microscopy (TEM) characterization was carried out on a Zeiss Libra 120 (Carl Zeiss, Jena, Germany) operating at 120 kV. High-resolution TEM (HRTEM) and scanning TEM (STEM) were measured using a field emission gun FEI Tecnai F20 microscope at 200 kV. High-angle annular dark-field (HAADF) STEM was combined with electron energy loss spectroscopy (EELS) in the Tecnai microscope by using a

https://doi.org/10.1021/acsnano.2c03788
ACS Nano 2022, 16, 11102–11114

GATAN QUANTUM filter. X-ray photoelectron spectroscopy (XPS) measurements were performed using an Al anode XR50 source operating at 150 mW and a Phoibos 150 MCD-9 detector. Thermogravimetric (TGA) (PerkinElmer Diamond TG/DTA Instruments) experiment was carried out to record the ratio of S within the prepared composites. UV−vis absorption spectra were identified by a PerkinElmer LAMBDA 950 UV−vis spectrophotometer. Nitrogen adsorption−desorption isotherms were recorded to calculate the specific surface area and analysis of the pore size distribution by the Brunauer−Emmett−Teller method (Tristar II 3020 Micromeritics system). Electrical conductivities were measured using a four-point probe station (Keithley 2400, Tektronix). Electron paramagnetic resonance (EPR) spectra were acquired on a Bruker EMXmicro spectrometer.

Electrochemical Measurements. LSB performance was tested at room temperature in CR2032 coin-type cells. Active materials (S/$Cu_{1.8}Se$, S/Cu_2Se, and S/Super P), PVDF binders, and Super P were mixed (weight ratio = 8:1:1) in NMP to form a black slurry and then coated on Al foils and dried at 60 °C overnight. The prepared homogeneous slurry was coated on an aluminum foil and vacuum-dried at 60 °C overnight. Subsequently, the coated aluminum foil was punched into small disks with a diameter of 12.0 mm as the cathode. Sulfur loading was about 1.0 mg cm^{-2} (E/S = 20 μL mg^{-1}). Lithium foils were used as anode and Celgard 2400 membranes as separators. The electrolyte was prepared by dissolving 1.0 M lithium bis(trifluoromethanesulfonyl)imide in a mixture of DOL and DME (v/v = 1/1) with 0.2 M $LiNO_3$ additive. Galvanostatic charge−discharge (GCD) tests were performed on a Neware BTS4008 battery tester with different C rates. Cyclic voltammetry (CV) measurements were performed on a battery tester BCS-810 from Bio Logic at a scan rate of 0.1−0.4 mV $s^{-1}$with an electrochemical window of 1.7−2.8 V, and electrochemical impedance spectroscopy (EIS) tests with a voltage amplitude of 10 mV in the frequency range 100 kHz to 0.01 Hz were performed.

Preparation of Li_2S_4 Solutions for Adsorption Test. Sulfur and Li_2S with a molar ratio of 3:1 were dissolved into a certain amount of DME and DOL (volume ratio of 1:1) for continuous stirring overnight in a glovebox, which eventually yielded a homogeneous dark brown solution. To evaluate the polysulfide absorption ability, 15 mg of each $Cu_{1.8}Se$, Cu_2Se, and Super P was poured into 3.0 mL of 10 mM Li_2S_4 solution, respectively. The obtained mixtures were vigorously stirred for 2 h and aged overnight under an Ar atmosphere.

Symmetric Cell Assembly and Measurements. Symmetric cells were assembled and tested using the same process as for LSBs. Two pieces of the same electrode (average S loading about 0.5 mg cm^{-2}) were used as identical working and counter electrodes. Each coin cell contained 40 μL of electrolyte (0.5 M Li_2S_6 and 1 M LiTFSI in 1:1 DOL/DME (v/v)). CV measurements were carried out at a scan rate of 20 mV s^{-1}.

Measurement of Nucleation of Li_2S. Standard 2032 coin cells were assembled to analyze the nucleation of Li_2S. A certain amount of host materials ($Cu_{1.8}Se$ and Cu_2Se) were dissolved in ethanol. Then, the catalysts were coated on the carbon papers applied as the working electrode. Li foil worked as the counter electrode. The catholyte consisted of 20 μL of 0.25 M Li_2S_8 dissolved in tetraglyme with 1.0 M LiTFSI. The anolyte contained 20 μL of 1.0 M LiTFSI in tetraglyme solution without Li_2S_8. The cells were first discharged at a current of 0.112 mA to 2.06 V, and then, the voltage was held at 2.05 V until the current decreased to 0.01 mA for Li_2S nucleation and growth.

ASSOCIATED CONTENT

Supporting Information

The Supporting Information is available free of charge at https://pubs.acs.org/doi/10.1021/acsnano.2c03788.

Discussion of theoretical calculations details, figures of STEM images, EELS chemical compostition maps, HAADF STEM images, HRTEM images, EPR spectra, electrical conductivity, XRD pattern, nitrogen adsorption−desorption isotherms, BET surface areas, TGA profile, DFT calculation results, CV curves, charge and discharge profiles, EIS spectra, equivalent circuit before and after cycling, and resistance of the insulating Li_2S_2/Li_2S layer, and table of summary of the comparison of $Cu_{1.8}Se$ electrochemical performance as host cathode for LSBs with state-of-the-art Cu-based or Se-based materials (PDF)

AUTHOR INFORMATION

Corresponding Authors

Mengyao Li − *Catalonia Institute for Energy Research − IREC, 08930 Barcelona, Spain; Department of Electronic and Biomedical Engineering, Universitat de Barcelona, 08028 Barcelona, Spain; School of Physics and Microelectronics, Zhengzhou University, Zhengzhou 450052, China;* orcid.org/0000-0002-9082-7938; Email: limengyao@irec.cat

Jiaao Wang − *Department of Chemistry and the Oden Institute for Computational Engineering and Sciences, The University of Texas at Austin, Austin, Texas 78712, United States;* Email: wangjiaao0720@utexas.edu

David Mitlin − *Materials Science and Engineering Program & Texas Materials Institute, The University of Texas at Austin, Austin, Texas 78712, United States;* Email: david.mitlin2@utexas.edu

Shulei Chou − *Institute for Carbon Neutralization, College of Chemistry and Materials Engineering, Wenzhou University, Wenzhou, Zhejiang 325035, China;* orcid.org/0000-0003-1155-6082; Email: chou@wzu.edu.cn

Andreu Cabot − *Catalonia Institute for Energy Research − IREC, 08930 Barcelona, Spain; ICREA, 08010 Barcelona, Spain;* orcid.org/0000-0002-7533-3251; Email: acabot@irec.cat

Authors

Dawei Yang − *Catalonia Institute for Energy Research − IREC, 08930 Barcelona, Spain; Department of Electronic and Biomedical Engineering, Universitat de Barcelona, 08028 Barcelona, Spain; Henan Key Laboratory of Photovoltaic Materials, Henan University, Kaifeng 475004, China;* orcid.org/0000-0002-3842-8286

Xuejiao Zheng − *Nanjing Hydraulic Research Institute, Nanjing 210029, China*

Xu Han − *Catalan Institute of Nanoscience and Nanotechnology (ICN2), CSIC and BIST, 08193 Barcelona, Spain*

Chaoqi Zhang − *Catalonia Institute for Energy Research − IREC, 08930 Barcelona, Spain; Department of Electronic and Biomedical Engineering, Universitat de Barcelona, 08028 Barcelona, Spain;* orcid.org/0000-0002-0357-235X

Jordi Jacas Biendicho − *Catalonia Institute for Energy Research − IREC, 08930 Barcelona, Spain;* orcid.org/0000-0001-5981-6168

Jordi Llorca − *Institute of Energy Technologies, Department of Chemical Engineering and Barcelona Research Center in Multiscale Science and Engineering, Universitat Politècnica de Catalunya, EEBE, 08019 Barcelona, Spain;* orcid.org/0000-0002-7447-9582

Hongchang Hao − *Materials Science and Engineering Program & Texas Materials Institute, The University of*

https://doi.org/10.1021/acsnano.2c03788
ACS Nano 2022, 16, 11102−11114

Texas at Austin, Austin, Texas 78712, United States; orcid.org/0000-0003-4190-4105

Junshan Li – *Institute of Advanced Study, Chengdu University, 610106 Chengdu, China;* orcid.org/0000-0002-1482-1972

Graeme Henkelman – *Department of Chemistry and the Oden Institute for Computational Engineering and Sciences, The University of Texas at Austin, Austin, Texas 78712, United States;* orcid.org/0000-0002-0336-7153

Jordi Arbiol – *Catalan Institute of Nanoscience and Nanotechnology (ICN2), CSIC and BIST, 08193 Barcelona, Spain; ICREA, 08010 Barcelona, Spain;* orcid.org/0000-0002-0695-1726

Joan Ramon Morante – *Catalonia Institute for Energy Research – IREC, 08930 Barcelona, Spain; Department of Electronic and Biomedical Engineering, Universitat de Barcelona, 08028 Barcelona, Spain*

Complete contact information is available at: https://pubs.acs.org/10.1021/acsnano.2c03788

Notes

The authors declare no competing financial interest.

ACKNOWLEDGMENTS

The authors thank the support from the projects ENE2016-77798-C4-3-R and NANOGEN (PID2020-116093RB-C43), funded by MCIN/AEI/10.13039/501100011033/and by "ERDF A way of making Europe", by the "European Union". D.Y., M.L., X.H., and C.Z. thank the China Scholarship Council for the scholarship support. ICN2 acknowledges the support from the Severo Ochoa Programme (MINECO, grant no. SEV-2017-0706). IREC and ICN2 are both funded by the CERCA Program/Generalitat de Catalunya. This project received funding from the European Union's Horizon 2020 research and innovation program under grant agreement No. 823717-ESTEEM3. Calculations at UT Austin were supported by the Welch Foundation (F-1841) and the Texas Advanced Computing Center. Part of the present work has been performed in the framework of Universitat Autònoma de Barcelona Materials Science PhD program. J.L. is a Serra Húnter Fellow and is grateful to MICINN/FEDER RTI2018-093996-B-C31, GC 2017 SGR 128, and to the ICREA Academia program.

REFERENCES

(1) Bai, S.; Liu, X.; Zhu, K.; Wu, S.; Zhou, H. Metal-Organic Framework-Based Separator for Lithium-Sulfur Batteries. *Nat. Energy* **2016**, *1*, 16049.

(2) Chou, S.; Dou, S. Next-Generation Batteries. *Adv. Mater.* **2017**, *29* (48), 1705871.

(3) Seh, Z. W.; Sun, Y.; Zhang, Q.; Cui, Y. Designing High-Energy Lithium-Sulfur Batteries. *Chem. Soc. Rev.* **2016**, *45* (20), 5605–5634.

(4) Bruce, P. G.; Freunberger, S. A.; Hardwick, L. J.; Tarascon, J. M. $LigO_2$ and LigS Batteries with High Energy Storage. *Nat. Mater.* **2012**, *11* (1), 19–29.

(5) Manthiram, A.; Fu, Y.; Chung, S. H.; Zu, C.; Su, Y. S. Rechargeable Lithium-Sulfur Batteries. *Chem. Rev.* **2014**, *114* (23), 11751–11787.

(6) Li, Z.; Wu, H. B.; Lou, X. W. Rational Designs and Engineering of Hollow Micro-/Nanostructures as Sulfur Hosts for Advanced Lithium-Sulfur Batteries. *Energy Environ. Sci.* **2016**, *9* (10), 3061–3070.

(7) Liang, X.; Rangom, Y.; Kwok, C. Y.; Pang, Q.; Nazar, L. F. Interwoven MXene Nanosheet/Carbon-Nanotube Composites as Li–S Cathode Hosts. *Adv. Mater.* **2017**, *29* (3), 1603040.

(8) Xu, F.; Tang, Z.; Huang, S.; Chen, L.; Liang, Y.; Mai, W.; Zhong, H.; Fu, R.; Wu, D. Facile Synthesis of Ultrahigh-Surface-Area Hollow Carbon Nanospheres for Enhanced Adsorption and Energy Storage. *Nat. Commun.* **2015**, *6*, 7221.

(9) Du, Z.; Chen, X.; Hu, W.; Chuang, C.; Xie, S.; Hu, A.; Yan, W.; Kong, X.; Wu, X.; Ji, H.; Wan, L. J. Cobalt in Nitrogen-Doped Graphene as Single-Atom Catalyst for High-Sulfur Content Lithium-Sulfur Batteries. *J. Am. Chem. Soc.* **2019**, *141* (9), 3977–3985.

(10) Schuster, J.; He, G.; Mandlmeier, B.; Yim, T.; Lee, K. T.; Bein, T.; Nazar, L. F. Spherical Ordered Mesoporous Carbon Nanoparticles with High Porosity for Lithium-Sulfur Batteries. *Angew. Chem., Int. Ed.* **2012**, *51* (15), 3591–3595.

(11) Shi, J. Le; Tang, C.; Huang, J. Q.; Zhu, W.; Zhang, Q. Effective Exposure of Nitrogen Heteroatoms in 3D Porous Graphene Framework for Oxygen Reduction Reaction and Lithium–Sulfur Batteries. *J. Energy Chem.* **2018**, *27* (1), 167–175.

(12) He, Y.; Li, M.; Zhang, Y.; Shan, Z.; Zhao, Y.; Li, J.; Liu, G.; Liang, C.; Bakenov, Z.; Li, Q. All-Purpose Electrode Design of Flexible Conductive Scaffold toward High-Performance Li–S Batteries. *Adv. Funct. Mater.* **2020**, *30* (19), 2000613.

(13) Hou, W.; Feng, P.; Guo, X.; Wang, Z.; Bai, Z.; Bai, Y.; Wang, G.; Sun, K. Catalytic Mechanism of Oxygen Vacancies in Perovskite Oxides for Lithium–Sulfur Batteries. *Adv. Mater.* **2022**, 2202222.

(14) Wang, X.; Li, G.; Li, J.; Zhang, Y.; Wook, A.; Yu, A.; Chen, Z. Structural and Chemical Synergistic Encapsulation of Polysulfides Enables Ultralong-Life Lithium-Sulfur Batteries. *Energy Environ. Sci.* **2016**, *9* (8), 2533–2538.

(15) Liang, X.; Hart, C.; Pang, Q.; Garsuch, A.; Weiss, T.; Nazar, L. F. A Highly Efficient Polysulfide Mediator for Lithium–Sulfur Batteries. *Nat. Commun.* **2015**, *6*, 5682.

(16) Cui, Z.; Zu, C.; Zhou, W.; Manthiram, A.; Goodenough, J. B. Mesoporous Titanium Nitride-Enabled Highly Stable Lithium-Sulfur Batteries. *Adv. Mater.* **2016**, *28* (32), 6926–6931.

(17) Zhong, Y.; Yin, L.; He, P.; Liu, W.; Wu, Z.; Wang, H. Surface Chemistry in Cobalt Phosphide-Stabilized Lithium-Sulfur Batteries. *J. Am. Chem. Soc.* **2018**, *140* (4), 1455–1459.

(18) Wang, J.; Zhao, Y.; Li, G.; Luo, D.; Liu, J.; Zhang, Y.; Wang, X.; Shui, L.; Chen, Z. Aligned Sulfur-Deficient ZnS_{1-x} Nanotube Arrays as Efficient Catalyzer for High-Performance Lithium/Sulfur Batteries. *Nano Energy* **2021**, *84*, 105891.

(19) Liu, X.; He, Q.; Yuan, H.; Yan, C.; Zhao, Y.; Xu, X.; Huang, J. Q.; Chueh, Y. L.; Zhang, Q.; Mai, L. Interface Enhanced Well-Dispersed Co_9S_8 Nanocrystals as an Efficient Polysulfide Host in Lithium–Sulfur Batteries. *J. Energy Chem.* **2020**, *48*, 109–115.

(20) Lin, H.; Yang, L.; Jiang, X.; Li, G.; Zhang, T.; Yao, Q.; Zheng, G. W.; Lee, J. Y. Electrocatalysis of Polysulfide Conversion by Sulfur-Deficient MoS_2 Nanoflakes for Lithium-Sulfur Batteries. *Energy Environ. Sci.* **2017**, *10*, 1476–1486.

(21) Lei, T.; Chen, W.; Huang, J.; Yan, C.; Sun, H.; Wang, C.; Zhang, W.; Li, Y.; Xiong, J. Multi-Functional Layered WS_2 Nanosheets for Enhancing the Performance of Lithium–Sulfur Batteries. *Adv. Energy Mater.* **2017**, *7* (4), 1601843.

(22) Wang, S.; Zhao, S.; Guo, X.; Wang, G. 2D Material-Based Heterostructures for Rechargeable Batteries. *Adv. Energy Mater.* **2022**, *12* (4), 2100864.

(23) Wang, Y.; Yang, D.; Lian, J.; Wei, T.; Sun, Y. Ordered Corn-like $CuCo_2O_4$ Nanoforests Covering Ni Foam for a High-Performance All-Solid-State Supercapacitor. *J. Alloys Compd.* **2018**, *741*, 527–531.

(24) Xin, X.; Song, Y.; Guo, S.; Zhang, Y.; Wang, B.; Yu, J.; Li, X. In-Situ Growth of High-Content 1T Phase MoS_2 Confined in the CuS Nanoframe for Efficient Photocatalytic Hydrogen Evolution. *Appl. Catal. B Environ.* **2020**, *269*, 118773.

(25) Li, M.; Liu, Y.; Zhang, Y.; Han, X.; Zhang, T.; Zuo, Y.; Xie, C.; Xiao, K.; Arbiol, J.; Llorca, J.; Ibáñez, M.; Liu, J.; Cabot, A. Effect of the Annealing Atmosphere on Crystal Phase and Thermoelectric Properties of Copper Sulfide. *ACS Nano* **2021**, *15* (3), 4967–4978.

(26) Coughlan, C.; Ibáñez, M.; Dobrozhan, O.; Singh, A.; Cabot, A.; Ryan, K. M. Compound Copper Chalcogenide Nanocrystals. *Chem. Rev.* **2017**, *117* (9), 5865−6109.
(27) Chen, H.; Fang, C.; Gao, X.; Jiang, G.; Wang, X.; Sun, S. P.; Duo Wu, W.; Wu, Z. Sintering- and Oxidation-Resistant Ultrasmall Cu(I)/(II) Oxides Supported on Defect-Rich Mesoporous Alumina Microspheres Boosting Catalytic Ozonation. *J. Colloid Interface Sci.* **2021**, *581*, 964−978.
(28) Yang, D.; Zhu, Q.; Chen, C.; Liu, H.; Liu, Z.; Zhao, Z.; Zhang, X.; Liu, S.; Han, B. Selective Electroreduction of Carbon Dioxide to Methanol on Copper Selenide Nanocatalysts. *Nat. Commun.* **2019**, *10* (1), 677.
(29) Chen, H.; Gao, Y.; Ye, L.; Yao, Y.; Chen, X.; Wei, Y.; Sun, L. A Cu_2Se-Cu_2O Film Electrodeposited on Titanium Foil as a Highly Active and Stable Electrocatalyst for the Oxygen Evolution Reaction. *Chem. Commun.* **2018**, *54* (39), 4979−4982.
(30) Yu, Q.; Lu, Y.; Luo, R.; Liu, X.; Huo, K.; Kim, J. K.; He, J.; Luo, Y. In Situ Formation of Copper-Based Hosts Embedded within 3D N-Doped Hierarchically Porous Carbon Networks for Ultralong Cycle Lithium−Sulfur Batteries. *Adv. Funct. Mater.* **2018**, *28* (39), 1804520.
(31) Sun, K.; Su, D.; Zhang, Q.; Bock, D. C.; Marschilok, A. C.; Takeuchi, K. J.; Takeuchi, E. S.; Gan, H. Interaction of CuS and Sulfur in Li-S Battery System. *J. Electrochem. Soc.* **2015**, *162* (14), A2834−A2839.
(32) Hosseini, S. M.; Varzi, A.; Ito, S.; Aihara, Y.; Passerini, S. High Loading CuS-Based Cathodes for All-Solid-State Lithium Sulfur Batteries with Enhanced Volumetric Capacity. *Energy Storage Mater.* **2020**, *27*, 61−68.
(33) He, D.; Xue, P.; Song, D.; Qu, J.; Lai, C. Tri-Functional Copper Sulfide as Sulfur Carrier for High-Performance Lithium-Sulfur Batteries. *J. Electrochem. Soc.* **2017**, *164* (7), A1499−A1502.
(34) Li, X.; Lv, W.; Wu, G.; Fu, G.; Zhang, W.; Li, Z. A Novel CuSe-$Cu_{1.8}Se$ Heterostructure with Hexahedral Structure Cathode Material for Aluminum Batteries. *Chem. Eng. J.* **2021**, *426*, 131899.
(35) Gao, F.; Zhu, L.; Wang, Y.; Xie, H.; Li, J. Room Temperature Facile Synthesis of Cu_2Se Hexagonal Nanoplates Array Film and Its High Photodegradation Activity to Methyl Blue with the Assistance of H_2O_2. *Mater. Lett.* **2016**, *183*, 425−428.
(36) Li, W.; Ma, Y.; Li, P.; Jing, X.; Jiang, K.; Wang, D. Electrochemically Activated $Cu_{2-x}Te$ as an Ultraflat Discharge Plateau, Low Reaction Potential, and Stable Anode Material for Aqueous Zn-Ion Half and Full Batteries. *Adv. Energy Mater.* **2021**, *11* (42), 2102607.
(37) Zhang, D. M.; Jia, J. H.; Yang, C. C.; Jiang, Q. Fe_7Se_8 Nanoparticles Anchored on N-Doped Carbon Nanofibers as High-Rate Anode for Sodium-Ion Batteries. *Energy Storage Mater.* **2020**, *24*, 439−449.
(38) Yang, D.; Liang, Z.; Zhang, C.; Biendicho, J. J.; Botifoll, M.; Spadaro, M. C.; Chen, Q.; Li, M.; Ramon, A.; Moghaddam, A. O.; Llorca, J.; Wang, J.; Morante, J. R.; Arbiol, J.; Chou, S. L.; Cabot, A. $NbSe_2$ Meets C_2N: A 2D-2D Heterostructure Catalysts as Multifunctional Polysulfide Mediator in Ultra-Long-Life Lithium−Sulfur Batteries. *Adv. Energy Mater.* **2021**, *11* (36), 2101250.
(39) Guo, Q.; Li, S.; Liu, X.; Lu, H.; Chang, X.; Zhang, H.; Zhu, X.; Xia, Q.; Yan, C.; Xia, H. Ultrastable Sodium−Sulfur Batteries without Polysulfides Formation Using Slit Ultramicropore Carbon Carrier. *Adv. Sci.* **2020**, *7* (11), 1903246.
(40) Yang, D.; Zhang, C.; Biendicho, J. J.; Han, X.; Liang, Z.; Du, R.; Li, M.; Li, J.; Arbiol, J.; Llorca, J.; Zhou, Y.; Morante, J. R.; Cabot, A. ZnSe/N-Doped Carbon Nanoreactor with Multiple Adsorption Sites for Stable Lithium-Sulfur Batteries. *ACS Nano* **2020**, *14* (11), 15492−15504.
(41) Shi, H.; Qin, J.; Lu, P.; Dong, C.; He, J.; Chou, X.; Das, P.; Wang, J.; Zhang, L.; Wu, Z. S. Interfacial Engineering of Bifunctional Niobium (V)-Based Heterostructure Nanosheet Toward High Efficiency Lean-Electrolyte Lithium−Sulfur Full Batteries. *Adv. Funct. Mater.* **2021**, *31* (28), 2102314.
(42) Luo, D.; Li, G.; Deng, Y. P.; Zhang, Z.; Li, J.; Liang, R.; Li, M.; Jiang, Y.; Zhang, W.; Liu, Y.; Lei, W.; Yu, A.; Chen, Z. Synergistic Engineering of Defects and Architecture in Binary Metal Chalcogenide toward Fast and Reliable Lithium−Sulfur Batteries. *Adv. Energy Mater.* **2019**, *9* (18), 1900228.
(43) Cai, D.; Liu, B.; Zhu, D.; Chen, D.; Lu, M.; Cao, J.; Wang, Y.; Huang, W.; Shao, Y.; Tu, H.; Han, W. Ultrafine Co_3Se_4 Nanoparticles in Nitrogen-Doped 3D Carbon Matrix for High-Stable and Long-Cycle-Life Lithium Sulfur Batteries. *Adv. Energy Mater.* **2020**, *10* (19), 1904273.
(44) Ci, H.; Cai, J.; Ma, H.; Shi, Z.; Cui, G.; Wang, M.; Jin, J.; Wei, N.; Lu, C.; Zhao, W.; Sun, J.; Liu, Z. Defective VSe_2-Graphene Heterostructures Enabling In Situ Electrocatalyst Evolution for Lithium-Sulfur Batteries. *ACS Nano* **2020**, *14* (9), 11929−11938.
(45) Tian, Y.; Li, G.; Zhang, Y.; Luo, D.; Wang, X.; Zhao, Y.; Liu, H.; Ji, P.; Du, X.; Li, J.; Chen, Z. Low-Bandgap Se-Deficient Antimony Selenide as a Multifunctional Polysulfide Barrier toward High-Performance Lithium−Sulfur Batteries. *Adv. Mater.* **2020**, *32* (4), 1904876.
(46) Wang, J.; Cao, S.; Yang, L.; Zhang, Y.; Xing, K.; Lu, X.; Xu, J. Metastable Marcasite $NiSe_2$ Nanodendrites on Carbon Fiber Clothes to Suppress Polysulfide Shuttling for High-Performance Lithium−Sulfur Batteries. *Nanoscale* **2021**, *13* (39), 16487−16498.
(47) Wang, L.; Ni, Y.; Hou, X.; Chen, L.; Li, F.; Chen, J. A Two-Dimensional Metal-Organic Polymer Enabled by Robust Nickel-Nitrogen and Hydrogen Bonds for Exceptional Sodiun-Ion Storage. *Angew. Chem., Int. Ed.* **2020**, *59* (49), 22126−22131.
(48) Li, Y.; Wang, W.; Zhang, B.; Fu, L.; Wan, M.; Li, G.; Cai, Z.; Tu, S.; Duan, X.; Seh, Z. W.; Jiang, J.; Sun, Y. Manipulating Redox Kinetics of Sulfur Species Using Mott-Schottky Electrocatalysts for Advanced Lithium-Sulfur Batteries. *Nano Lett.* **2021**, *21* (15), 6656−6663.
(49) Zhang, L.; Liu, D.; Muhammad, Z.; Wan, F.; Xie, W.; Wang, Y.; Song, L.; Niu, Z.; Chen, J. Single Nickel Atoms on Nitrogen-Doped Graphene Enabling Enhanced Kinetics of Lithium−Sulfur Batteries. *Adv. Mater.* **2019**, *31* (40), 1903955.
(50) Xu, J.; Zhang, W.; Fan, H.; Cheng, F.; Su, D.; Wang, G. Promoting Lithium Polysulfide/Sulfide Redox Kinetics by the Catalyzing of Zinc Sulfide for High Performance Lithium-Sulfur Battery. *Nano Energy* **2018**, *51*, 73−82.
(51) Song, Y.; Zhao, W.; Kong, L.; Zhang, L.; Zhu, X.; Shao, Y.; Ding, F.; Zhang, Q.; Sun, J.; Liu, Z. Synchronous Immobilization and Conversion of Polysulfides on VO_2-VN Binary Host Targeting High Sulfur Loading Li-S Batteries. *Energy Environ. Sci.* **2018**, *11* (9), 2620−2630.
(52) Zhang, C.; Du, R.; Biendicho, J. J.; Yi, M.; Xiao, K.; Yang, D.; Zhang, T.; Wang, X.; Arbiol, J.; Llorca, J.; Zhou, Y.; Morante, J. R.; Cabot, A. Tubular CoFeP@CN as a Mott−Schottky Catalyst with Multiple Adsorption Sites for Robust Lithium−Sulfur Batteries. *Adv. Energy Mater.* **2021**, *11* (24), 2100432.
(53) Zhao, H.; Tian, B.; Su, C.; Li, Y. Single-Atom Iron and Doped Sulfur Improve the Catalysis of Polysulfide Conversion for Obtaining High-Performance Lithium-Sulfur Batteries. *ACS Appl. Mater. Interfaces* **2021**, *13* (6), 7171−7177.
(54) Cai, D.; Lu, M.; Li, L.; Cao, J.; Chen, D.; Tu, H.; Li, J.; Han, W. A Highly Conductive MOF of Graphene Analogue $Ni_3(HITP)_2$ as a Sulfur Host for High-Performance Lithium−Sulfur Batteries. *Small* **2019**, *15* (44), 1970240.
(55) Liang, Z.; Yang, D.; Tang, P.; Zhang, C.; Biendicho, J. J.; Zhang, Y.; Llorca, J.; Wang, X.; Li, J.; Heggen, M.; David, J.; Dunin-Borkowski, R. E.; Zhou, Y.; Morante, J. R.; Cabot, A.; Arbiol, J. Atomically Dispersed Fe in a C_2N Based Catalyst as a Sulfur Host for Efficient Lithium−Sulfur Batteries. *Adv. Energy Mater.* **2021**, *11* (5), 2003507.
(56) Eftekhari, A. Energy Efficiency: A Critically Important but Neglected Factor in Battery Research. *Sustain. Energy Fuels* **2017**, *1* (10), 2053−2060.
(57) Shao, A. H.; Zhang, Z.; Xiong, D. G.; Yu, J.; Cai, J. X.; Yang, Z. Y. Facile Synthesis of a "Two-in-One" Sulfur Host Featuring Metallic-Cobalt-Embedded N-Doped Carbon Nanotubes for Efficient

https://doi.org/10.1021/acsnano.2c03788
ACS Nano 2022, 16, 11102−11114

Lithium-Sulfur Batteries. *ACS Appl. Mater. Interfaces* **2020**, *12* (5), 5968−5978.
(58) Baumann, A. E.; Aversa, G. E.; Roy, A.; Falk, M. L.; Bedford, N. M.; Thoi, V. S. Promoting Sulfur Adsorption Using Surface Cu Sites in Metal-Organic Frameworks for Lithium Sulfur Batteries. *J. Mater. Chem. A* **2018**, *6*, 4811−4821.
(59) Geng, P.; Du, M.; Guo, X.; Pang, H.; Tian, Z.; Braunstein, P.; Xu, Q. Bimetallic Metal-Organic Framework with High-Adsorption Capacity toward Lithium Polysulfides for Lithium−Sulfur Batteries. *Energy Environ. Mater.* **2021**, *5* (2), 599−607.
(60) Xiao, Z.; Yang, Z.; Zhang, L.; Pan, H.; Wang, R. Sandwich-Type NbS_2@S@I-Doped Graphene for High-Sulfur-Loaded, Ultrahigh-Rate and Long-Life Lithium-Sulfur Batteries. *ACS Nano* **2017**, *11* (8), 8488−8498.
(61) Hao, Q.; Cui, G.; Zhang, Y.; Li, J.; Zhang, Z. Novel $MoSe_2$/MoO_2 Heterostructure as an Effective Sulfur Host for High-Performance Lithium/Sulfur Batteries. *Chem. Eng. J.* **2020**, *381*, 122672.

https://doi.org/10.1021/acsnano.2c03788
ACS Nano 2022, 16, 11102−11114